Rare Met. (2023) 42(2):503–514
https://doi.org/10.1007/s12598-022-02180-1

RARE METALS

ORIGINAL ARTICLE

PdPbBi nanoalloys anchored reduced graphene-wrapped metal–organic framework-derived catalyst for enhancing ethylene glycol electrooxidation

Zhi-Rui Wu, Yu-Ting Zhong, Xiao-Guang Liu*, Ling Li*

Received: 1 July 2022 / Revised: 17 August 2022 / Accepted: 25 August 2022 / Published online: 7 November 2022

Abstract For future clean energy demand, it is essential to develop highly efficient and durable materials for use in renewable energy conversion devices. Herein, we report an electrocatalyst loaded with Pd-Pb-Bi nanoalloys on reduced graphene (rGO)-wrapped In_2O_3 (PdPbBi@rGO/In_2O_3) prepared by a hydrothermal method. PdPbBi@rGO/In_2O_3 exhibits higher forward current density (229.12 $mA\cdot cm^{-2}$), larger electrochemical active surface area (ECSA) (85.87 $m^2\cdot g^{-1}{}_{Pd}$), smaller impedance (12.68 Ω) and lower E_{onset} (−0.56 V) than commercial Pd/C. Specifically, the current density and ECSA are 8.46 and 3.38 times higher than those of commercial Pd/C (27.07 $mA\cdot cm^{-2}$, 25.41 $m^2\cdot g^{-1}{}_{Pd}$), respectively. Furthermore, the oxidation mechanism of ethylene glycol and the removal of carbon monoxide $[CO]_{ads}$ from the surface of Pd are also discussed in detail. The columnar support structure wrapped by rGO provides a huge active surface area for catalysis. Moreover, the electronic effect of Pd-Pb-Bi nanoalloys can accelerate the removal of CO intermediate species, obtain more Pd active sites and improve the electrocatalytic performance. Our first synthesis of this highly electrocatalyst offers promising value for commercial application in direct fuel cells.

Keywords Electrocatalyst; Pd-Pb-Bi nanoalloys; Ethylene glycol oxidation; In-MOF derivatives; Reduced graphene oxide

1 Introduction

The world's growing energy demand and fossil fuel consumption have correspondingly increased greenhouse gas emissions, driving the development of alternative energy sources with no or less pollution. Direct ethylene glycol fuel cells (DAFCs) have attracted much attention due to their high theoretical energy density, low environmental hazard, sufficient supply, renewability, and low volatility. Its commercialization has been an important research focus [1–3]. Rational design and fabrication of low-cost materials, strong carbon monoxide (CO) anti-toxicity, and long-term stability of anode electrodes are the keys to liquid fuel oxidation. However, the low oxidation kinetics, C–C bond cleavage during oxidation reactions, and the formation of polarized carbon-containing intermediates such as –COO, –CO, and –COOH on the catalyst surface severely hinder the commercialization of DAFCs [4, 5].

Indium oxide (In_2O_3) is widely used in various industries because of its excellent optical and electrical properties, non-toxicity and large activity [6, 7]. For example, it is used in lithium-ion batteries, dye-sensitized solar cells, and photocatalytic and gas sensors [8–12]. However, there are few research on the application of In_2O_3 in the electrocatalytic oxidation of ethylene glycol. Metal–organic frameworks (MOFs) are used as template precursors to synthesize different functional materials to form ordered and regular pore structures [13–15]. In another case, MOFs act as precursors and are converted to oxides upon high-

---

Supplementary Information The online version contains supplementary material available at https://doi.org/10.1007/s12598-022-02180-1.

Z.-R. Wu, Y.-T. Zhong, X.-G. Liu*, L. Li*
College of Chemistry and Chemical Engineering, Hubei University, Wuhan 430062, China
e-mail: liuxiaoguang402@hotmail.com

L. Li
e-mail: liling402431@hotmail.com

temperature calcination [16–18]. This open frame structure and strong interaction with guest oxide nanoparticles (NPs) have greatly enhanced catalytic performance in many fields [19]. However, the electrocatalytic performance of MOFs is limited because of their poor electrical conductivity [20, 21]. A facile way to improve electrical conductivity is to grow MOFs on conductive carbon materials such as graphene. For example, Yuan and co-workers [22] report a ZnSe–$FeSe_2$/RGO nanocomposite which enhances sodium/potassium storage. Nevertheless, due to the strong π–π interaction of graphene and its two-dimensional (2D) structure, it is hard to effectively expose all open metal-based active sites [14].

In the past few years, researchers have been focused on increasing the electrocatalytic active sites by doping metal atoms to improve the electrocatalytic performance of ethylene glycol oxidation reaction (EGOR) [23–25]. During EGOR, more C–C cleavage is required for complete oxidation. Several partially oxidized by-products are produced during this process, including glyoxal, glycolaldehyde, glycolic acid, oxalic acid, and glyoxylic acid [2, 26]. Complete oxidation of one EG molecule to CO_2 releases 10 electrons, producing a large amount of CO toxic intermediate [27]. This requires electrocatalysts with high activity and good CO resistance. Pd is cost-effective with high atomic efficiency and catalytic performance [28]. Recently, combining palladium with non-noble metal (Cu, Fe, Co, etc.) has been shown to be an effective strategy for the construction of bimetallic and even trimetallic palladium-based catalysts [29, 30]. In addition, the reported Pd alloys and compounds perform very well [31–34]. Besides, the introduction of oxophilic metals such as Pb can well promote the formation of surface-adsorbed OH substances ($[OH]_{ads}$) [35]. It can effectively convert CO-toxic intermediates on Pd to CO_2 at lower potentials, ultimately accelerating EGOR [36, 37]. At present, there are many kinds of electrocatalysts for metal and metal oxides, such as Cu-based bimetallic catalysts, $TiO_2/Ti_3C_2T_x$ MXene and $MoSe_2/Ti_3C_2T_x$ [38–40].

Herein, a three-dimensional (3D) columnar composite PdPbBi@rGO/In_2O_3 was first prepared by a simple hydrothermal, calcination and reduction method (Scheme 1). The obtained trimetallic catalyst (PdPbBi@rGO/In_2O_3) exhibits excellent electrochemical performance. The forward current density is 229.12 $mA \cdot cm^{-2}$, which is 8.46 times that of Pd/C (27.07 $mA \cdot cm^{-2}$). The electrochemical active surface area (ECSA) of PdPbBi@rGO/In_2O_3 is 85.87 $m^2 \cdot g^{-1}{}_{Pd}$, which is 3.38 times that of Pd/C (25.41 $m^2 \cdot g^{-1}{}_{Pd}$). In addition, PdPbBi@rGO/In_2O_3 has higher toxicity resistance and better stability to CO than commercial Pd/C. This new electrocatalyst offers inspiration for the commercial application of fuel cells.

2 Experimental

2.1 Synthesis of rGO/In_2O_3

Graphene oxide (GO) was prepared from graphite powder by modified Hummer's method [41, 42]. 0.27 g indium nitrate ($In(NO_3)_3 \cdot xH_2O$), 0.1980 g 1,3,5-benzentricarboxylic acid (H_3BTC), and 0.0495 g GO were added to a mixture of 3 ml H_2O and 12.4 ml N,N-dimethylformamide (DMF) and then stirred for 1 h. Then the mixed solution was poured into a 50 ml Teflon-lined autoclave and a hydrothermal reaction was performed at 120 °C for 5 days. After cooling, the obtained black product was filtered, washed three times alternately with distilled water, DMF and absolute ethanol, and dried under vacuum at 40 °C overnight. The resulting product was then calcined at 800 °C in a nitrogen atmosphere for 3 h. Finally, the precursor rGO/In_2O_3 was obtained.

2.2 Synthesis of PdPbBi@rGO/In_2O_3 electrocatalysts

50 mg rGO/In_2O_3 was disperses in EG (50 ml) by ultrasonication, then 5 ml palladium (II) chloride ($PdCl_2$) (0.0189 $mol \cdot L^{-1}$) was added to the above solution and stirred evenly. After that, 126 μl lead nitrate ($Pb(NO_3)_2$) (0.0756 $mol \cdot L^{-1}$) and 375.2 μl bismuth nitrate ($Bi(NO_3)_2 \cdot 5H_2O$) (0.0189 $mol \cdot L^{-1}$) were simultaneously added to the above solution under magnetic agitation. And the mixture was stirred at room temperature for 3 h. 80 mg sodium borohydride ($NaBH_4$) was dissolved in 20 ml distilled water, drop by drop into the mixed solution and stirred for 4 h. Then the product was collected by filtration, washed three times alternately with distilled water and ethanol, and dried overnight in 40 °C vacuum to obtain PdPbBi@rGO/In_2O_3. By the same procedure, PdPb@rGO/In_2O_3, PdBi@rGO/In_2O_3 and Pd@rGO/In_2O_3 electrocatalysts can also be synthesized without the addition of $Bi(NO_3)_2 \cdot 5H_2O$, $Pb(NO_3)_2$.

3 Results and discussion

3.1 Phase analysis

Structures of PdPbBi@rGO/In_2O_3, PdPb@rGO/In_2O_3, PdBi@rGO/In_2O_3, Pd@rGO/In_2O_3, rGO/In_2O_3 and In_2O_3 were analyzed by X-ray diffractometer (XRD) (Fig. 1a). The principal diffraction peaks of the support rGO/In_2O_3 at 2θ = 21.60°, 30.54°, 35.46°, 41.74°, 45.58°, 51.00°, 60.71° correspond to (211), (222), (400), (332), (134), (440), (622) planes of the In_2O_3 (ICDD No. 71-2195), indicating that In_2O_3 has been successfully synthesized [43, 44]. At

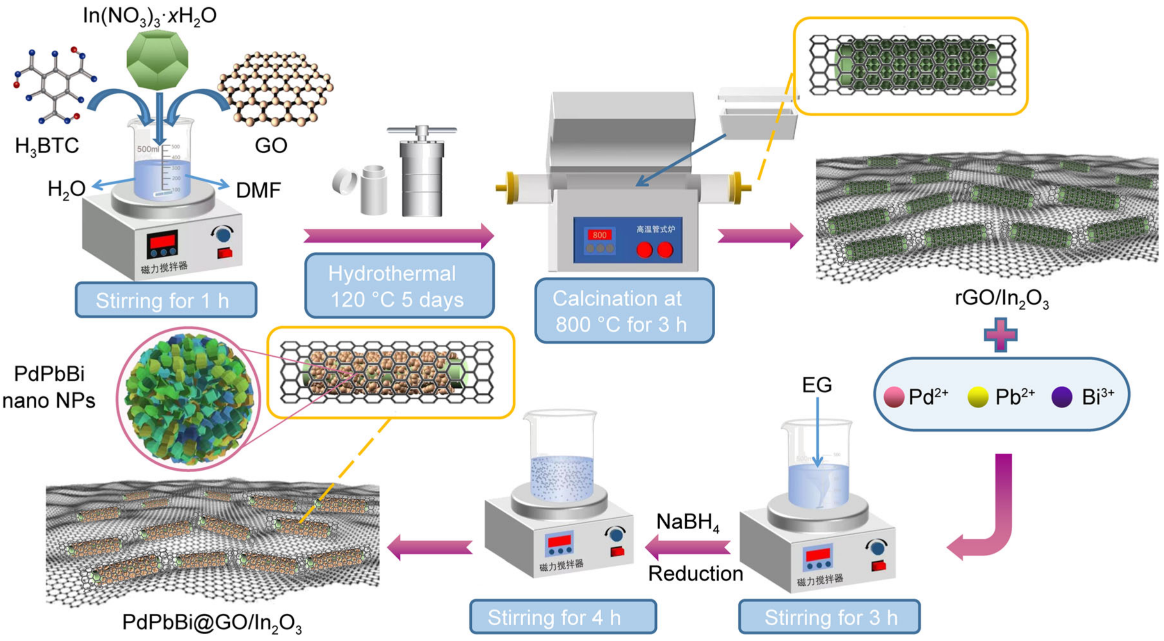

Scheme 1 Schematic diagram of preparation process of rGO/In_2O_3 electrocatalyst

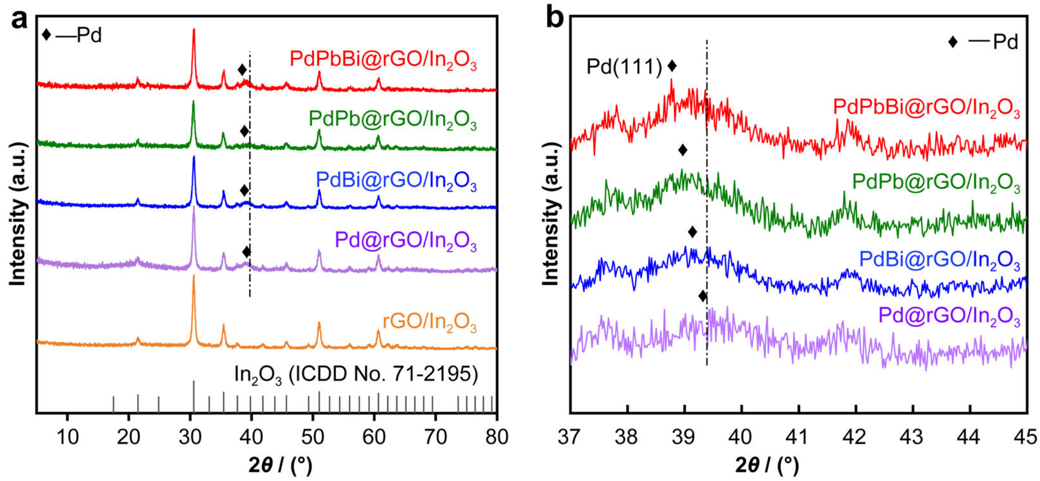

Fig. 1 **a** XRD patterns of $PdPbBi@rGO/In_2O_3$, $PdPb@rGO/In_2O_3$, $PdBi@rGO/In_2O_3$, $Pd@rGO/In_2O_3$, rGO/In_2O_3 and In_2O_3; **b** diffraction peaks of Pd in $PdPbBi@rGO/In_2O_3$, $PdPb@rGO/In_2O_3$, $PdBi@rGO/In_2O_3$ and $Pd@rGO/In_2O_3$

$2\theta = 25.0°$, the peak of In_2O_3 overlaps with the broad peaks of graphene, so that the (002) plane of graphene cannot be observed [45]. In addition, the diffraction peaks around 39.9° and 46.10° of the four catalysts belong to the (111) and (200) crystal planes of the face-centered cube (fcc) crystalline of Pd, respectively [42]. Figure 1b is the magnified XRD pattern. Compared with the diffraction angle of $Pd@rGO/In_2O_3$, the Pd (111) planes of $PdBi@rGO/In_2O_3$, $PdPb@rGO/In_2O_3$ and $PdPbBi@rGO/In_2O_3$ are shifted. The Pd (111) planes are shifted from 39.6° to 39.4°, 39.1° and 38.8°, respectively. This indicates that alloys have been formed between Pd, Pb and Bi [46, 47]. Furthermore, in the bimetallic PdPb, PdBi and trimetallic $PdPbBi@rGO/In_2O_3$ catalysts, due to the content of Pb and Bi, there are thin or amorphous phases, and no obvious Pb or Bi diffraction peaks are observed.

3.2 Morphology and composition analysis

Surface morphology of $PdPbBi@rGO/In_2O_3$ was investigated by field emission scanning electron microscopy (FESEM). Compared with rGO/In_2O_3 (Fig. 2a), the morphology of $PdPbBi@rGO/In_2O_3$ (Fig. 2b) is a prismatic surface covered with wrinkled rGO and metal NPs. Pd-Pb-Bi NPs are mostly uniformly spread over the surface of rGO/In_2O_3. By analyzing the elemental mapping in

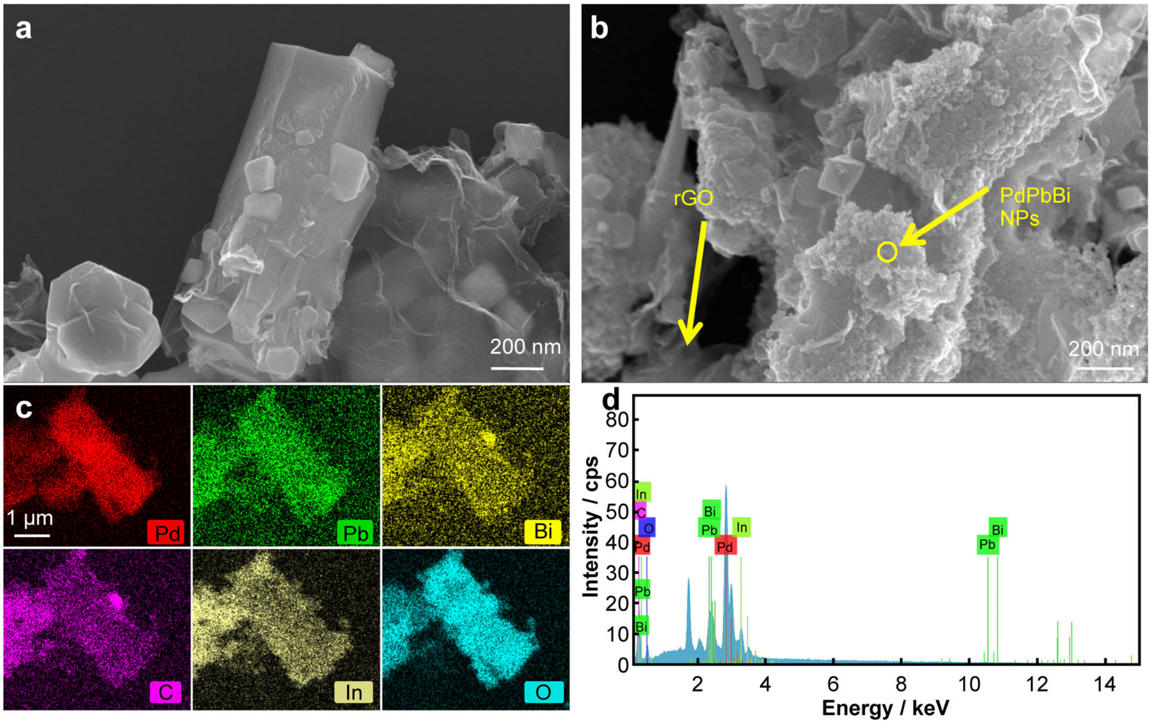

Fig. 2 FESEM images of **a** rGO/In_2O_3 and **b** PdPbBi@rGO/In_2O_3; **c** elemental mappings and **d** EDS results of PdPbBi@rGO/In_2O_3

Fig. 2c, we can further demonstrate that Pd, Pb, Bi, In and O are evenly distributed on the support rGO/In_2O_3. Energy dispersive X-ray spectrometer (EDS) spectrum (Fig. 2d) showed that the actual atomic loadings of Pd, Pb and Bi on the catalyst were 18.40%, 4.83% and 2.11%, respectively. The mass percentages of Pd, Pb and Bi measured by inductively coupled plasma optical emission spectrometer (ICP-OES) were 15.45%, 6.02% and 3.25%, respectively. The test results of both were close (Table S1), which was also in agreement with the initial addition ratio of the reactants. The above results indicate that PdPbBi@rGO/In_2O_3 has been successfully synthesized, and the PdPbBi NPs are uniformly dispersed on the surface of the support rGO/In_2O_3.

High-resolution transmission electron microscope (HRTEM) was used to further observe the morphology of PdPbBi@rGO/In_2O_3 (Fig. 3). In_2O_3 is a columnar structure with a length of about 2 μm (Fig. S1), which is consistent with SEM image. Figure 3a, b shows the crystalline properties of PdPbBi@rGO/In_2O_3. The lattice fringe spacing of 0.272 nm corresponds to the (222) plane of In_2O_3 in Fig. 3a. From the continuous lattice spacing we know that the crystal phase of In_2O_3 is pretty good. Figure 3b shows the well-shaped lattice stripes with interplanar spacing of 0.228 nm, corresponding to the (111) plane of Pd. Compared with pure Pd (0.223 nm), the interplanar spacing of Pd in the catalyst is slightly larger. The lattice of Pd expands with the addition of Pb and Bi NPs, confirming the formation of PdPbBi nanoalloys [48]. It is evident that most of the PdPbBi NPs are uniformly distributed on rGO/In_2O_3. More than 100 particles in Fig. 3c were randomly selected for statistical analysis to determine the size of the NPs. The statistical results in Fig. 3d show that the particle size of Pd-Pb-Bi alloy ranges from 1.5 to 7.5 nm, with an average particle size of (4.50 ± 0.86) nm. Smaller metal particles can better adsorb oxygenated substances, which is beneficial for the electrocatalytic oxidation of EG.

3.3 Analysis of elements and valence states

Valence state analysis of elements in PdPbBi@rGO/In_2O_3 was studied by X-ray photoelectron spectroscopy (XPS). The survey spectra show the photoelectron peaks of Pd, Pb, Bi, In, C and O in the trimetallic catalyst (Fig. S2). Pd 3d shows two asymmetric peaks, where binding energies (BEs) of Pd(0) $3d_{5/2}$ and Pd(0) $3d_{3/2}$ signals are detected at 335.3 and 340.8 eV (Fig. 4a) [49]. Figure 4b shows that the weak signal of Pb(II) is located at 138.3 eV ($4f_{7/2}$) and 143.2 eV ($4f_{5/2}$). Strong peaks of 137.0 and 141.9 eV correspond to Pb(0) $4f_{7/2}$ and Pb(0) $4f_{5/2}$, respectively, confirming that Pb exists in PdPbBi@rGO/In_2O_3 as elemental and divalent ions [50]. The BEs of 157.3 and 162.6 eV are assigned to Bi $4f_{7/2}$ and Bi $4f_{5/2}$ of Bi(0), respectively (Fig. 4c). Notably, the BE of Pd in PdPbBi@rGO/In_2O_3 shows slightly positive shifts compared to those of pure Pd (Pd $3d_{5/2}$ at 335.0 eV, Pd $3d_{3/2}$ at

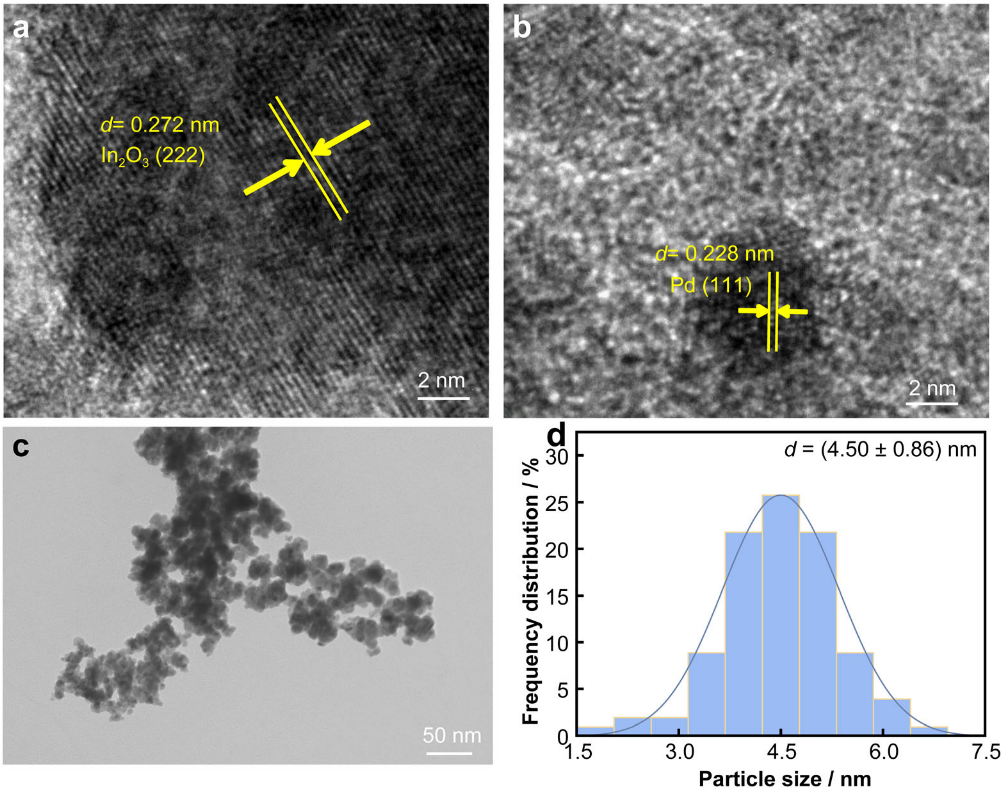

Fig. 3 HRTEM images of **a**–**c** PdPbBi@rGO/In_2O_3; **d** particle size distribution of Pd-Pb-Bi NPs

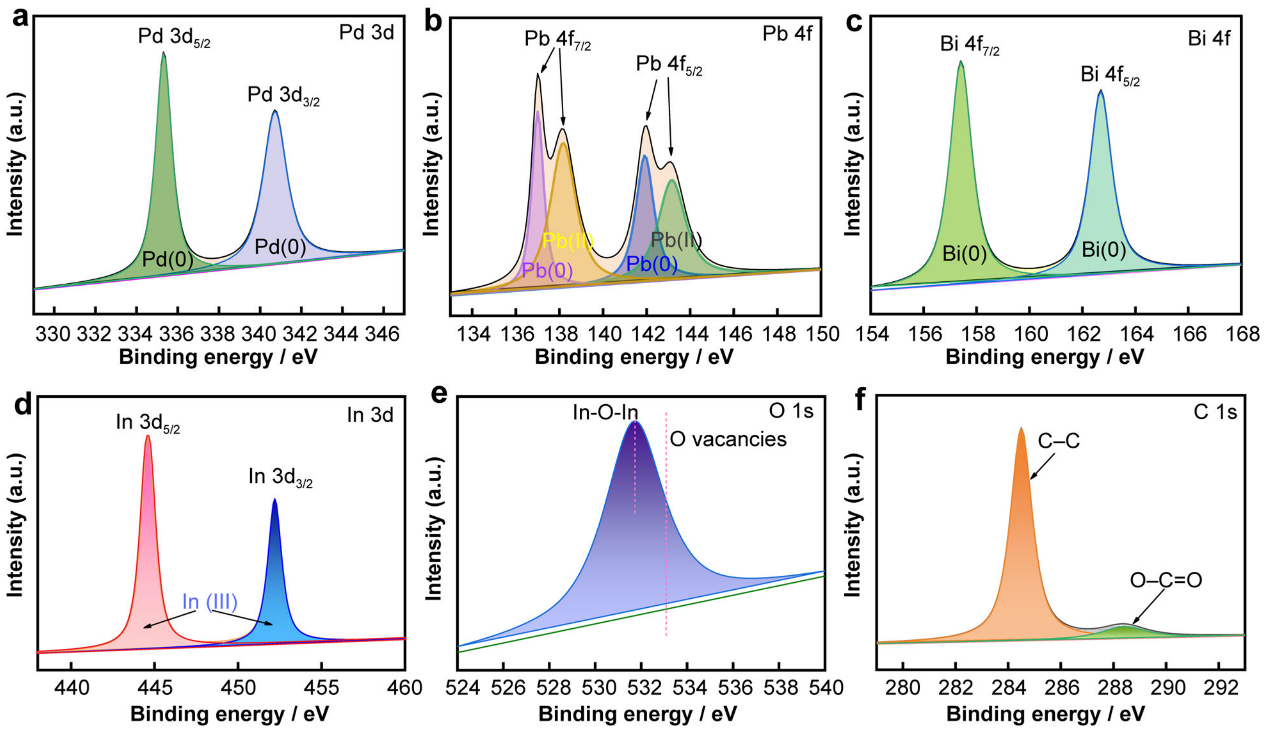

Fig. 4 XPS spectra of **a** Pd 3d, **b** Pb 4f, **c** Bi 4f, **d** In 3d, **e** O 1s and **f** C 1s in PdPbBi@rGO/In_2O_3

340.3 eV). This may be due to the fact that the incorporation of Pb and Bi affects the electronic structure of Pd, showing remarkable changes in the alloying phase, thereby improving the catalytic performance [28, 51]. Figure 4d depicts XPS spectrum of In 3d, showing two peaks at 444.8 and 452.3 eV. This can be attributed to the characteristic spin–orbit splitting of $3d_{5/2}$ and $3d_{3/2}$, respectively [52]. This proves that the valence state of indium in In_2O_3 is mainly + 3 [53]. Compared with pure In (In $3d_{5/2}$ at 443.8 eV, In $3d_{3/2}$ at 451.4 eV), the BE of In also shows slight positive shifts, indicating the interaction between In_2O_3 and rGO or metal NPs. The BE of O 1s is 531.8 eV compared to O vacancies (533.2 eV) (Fig. 4e) [54, 55]. This indicates the formation of In–O–In bonds in PdPbBi@rGO/In_2O_3 [56]. XPS spectrum of C 1s in Fig. 4f shows that there are two peaks, the prominent peak at 285.1 eV belongs to the C–C bond of rGO, another peak at 289.1 eV corresponds to the O–C=O functional group of rGO [57]. The peaks of oxygenated functional groups are particularly small, indicating that GO is reduced to rGO in the electrocatalyst.

3.4 Electrochemical performance analysis

In Fig. 5a, the anodic peaks between −0.1 and 0.5 V show the formation of PdO monolayer, Bi^{3+} and Pb^{2+} [58]. The reduction of Pd^{2+} to Pd, Pb to Pb^{2+} and Bi to Bi^{3+} results in apparent cathode peaks between −0.1 and 0.8 V [27]. According to the integral area of reduction peak (Fig. 6), the ECSAs of PdPbBi@rGO/In_2O_3, PdPb@rGO/In_2O_3, Pd@rGO/In_2O_3, PdBi@rGO/In_2O_3 and Pd/C are 85.87, 72.52, 60.48, 38.54 and 25.41 $m^2 \cdot g^{-1}{}_{Pd}$, respectively. The corresponding ECSAs data are listed in Table 1. The above results illustrate that the PdPbBi@rGO/In_2O_3 catalyst has more active centers and can absorb more oxygenated substances, thereby better promoting the electro-catalytic oxidation of EG. The EGOR performances of five catalysts were evaluated in 1.0 $mol \cdot L^{-1}$ KOH + 0.5 $mol \cdot L^{-1}$ EG (Fig. 5b). The cyclic voltammetry (CV) curve has two peaks, the peak with higher density at 0.5–0.7 V (forward scan) is designated as the ethylene glycol oxidation intermediate, and the other at 0–0.3 V (reverse scan) is the process by which intermediates such as CH_x and CO are further oxidized to CO_2 [1, 59]. The forward peak current densities ($I_{p,f}$) of PdPbBi@rGO/In_2O_3 (229.12 $mA \cdot cm^{-2}$) are 8.22, 1.73, 1.34 and 1.08 times higher than those of Pd/C (27.07 $mA \cdot cm^{-2}$), Pd@rGO/In_2O_3 (200.21 $mA \cdot cm^{-2}$), PdBi@rGO/In_2O_3 (172.27 $mA \cdot cm^{-2}$) and PdPb@rGO/In_2O_3 (162.61 $mA \cdot cm^{-2}$), respectively. The onset potential during electro-oxidation of EG (E_{onset}) of PdPbBi@rGO/In_2O_3 (−0.56 V) is smaller than those of PdPb@rGO/In_2O_3 (−0.51 V), PdBi@rGO/In_2O_3 (−0.50 V), Pd@rGO/In_2O_3

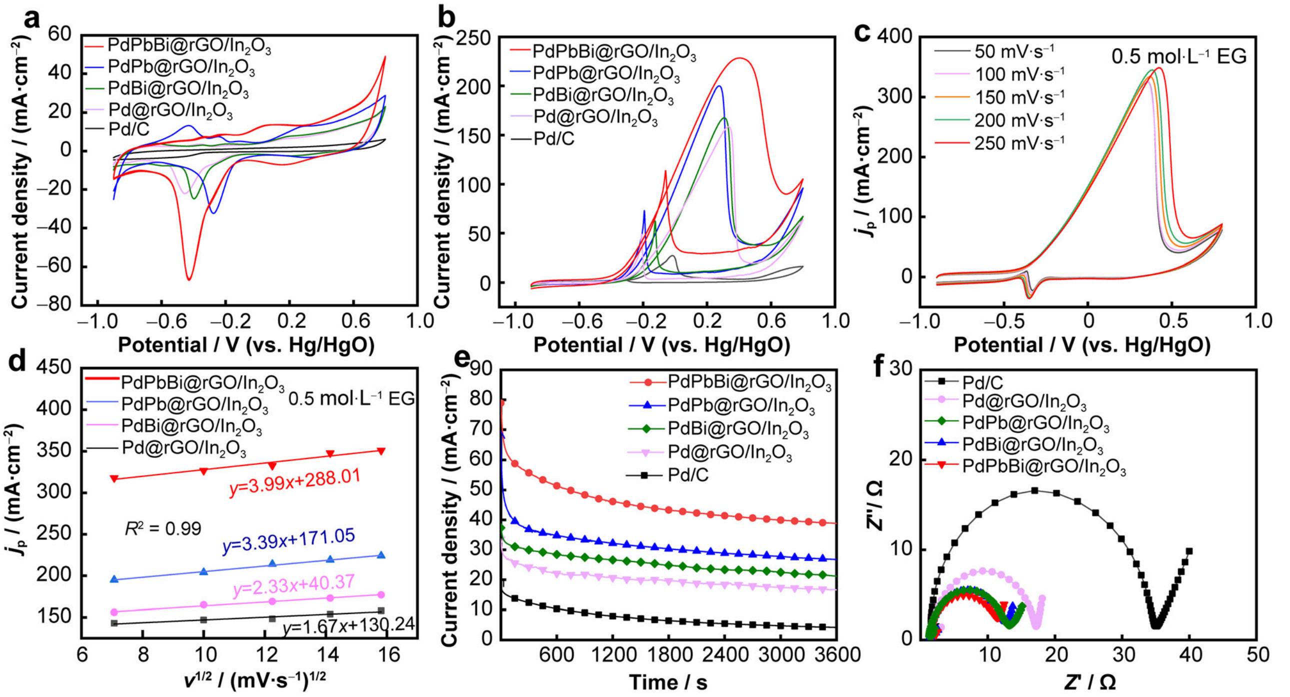

Fig. 5 CV curves of electrocatalysts in **a** 1.0 $mol \cdot L^{-1}$ KOH, **b** 1.0 $mol \cdot L^{-1}$ KOH + 0.5 $mol \cdot L^{-1}$ EG (scan rate: 50 $mV \cdot s^{-1}$); **c** EGOR curves of PdPbBi@rGO/In_2O_3 at various scan rates; **d** curves of peak current density (j_P) of four different catalysts and square root of scanning rate ($v^{1/2}$); **e** CA curves of five catalysts for 3600 s; **f** Nyquist plots of five catalysts

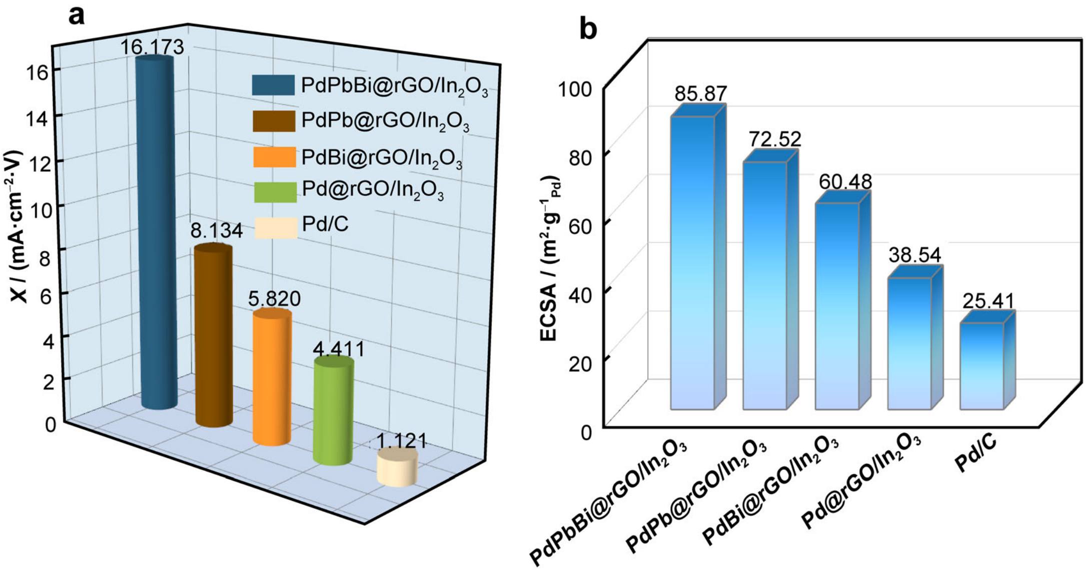

Fig. 6 **a** Integral area and **b** ECSA normalized area of five catalysts

Table 1 Results of CV measurements of all catalysts modified electrodes

Samples	ECSA^a / ($m^2 \cdot g^{-1}{}_{Pd}$)	$I_{p,\ f}{}^b$ / ($mA \cdot cm^{-2}$)	$E_{onset}{}^b$ / V	$I_{CA}{}^b$ / ($mA \cdot cm^{-2}$)	$R_{ct}{}^b$ / Ω
Pd/C	25.41	27.07	− 0.33	4.03	35.19
Pd@rGO/In_2O_3	38.54	162.61	− 0.48	19.43	18.88
PdBi@rGO/In_2O_3	60.48	172.27	− 0.50	23.79	17.17
PdPb@rGO/In_2O_3	72.52	200.21	− 0.51	33.79	13.19
PdPbBi@rGO/In_2O_3	85.87	229.12	− 0.56	40.47	12.68

a: in 1.0 $mol \cdot L^{-1}$ KOH; b: in 1.0 $mol \cdot L^{-1}$ KOH + 0.5 $mol \cdot L^{-1}$ EG

(−0.48 V) and Pd/C (−0.33 V). Meanwhile, the catalytic activity of the PdPbBi@rGO/In_2O_3 catalyst is significantly higher than that of the catalysts reported in other studies (Table S2).

We further investigated the kinetics of PdPbBi@rGO/In_2O_3 on catalytic EG oxidation (Fig. 5c). The peak current density (j_P) increases as the potential scanning rate increases from 50 to 250 $mV \cdot s^{-1}$, and the corresponding peak potential (V) shows a continuous positive shift. The square root of the scan rate ($v^{1/2}$) for four catalysts is linear with j_P (Fig. 5d). The diffusion correlation factor (R^2) of all lines is 0.99, indicating that the electro-oxidation reaction of each catalyst is an irreversible electrode process controlled by diffusion [60, 61]. The corresponding order of slope values is as follows: PdPbBi@rGO/In_2O_3 (3.99) > PdPb@rGO/In_2O_3 (3.39) > PdBi@rGO/In_2O_3 (2.33) > Pd@rGO/In_2O_3 (1.67). Higher slope values indicate better electrooxidation kinetics. The above results indicate that among all the catalysts, PdPbBi@rGO/In_2O_3 has the best kinetics for EGOR and the highest electrocatalytic activity.

To evaluate the EGOR stability of these five catalysts, we tested them in a solution containing 0.5 $mol \cdot L^{-1}$ EG + 1.0 $mol \cdot L^{-1}$ KOH at −0.1 V for 3600 s by chronoamperometry (CA). The current densities of all five catalysts show a significant decrease in the initial stage, and then decrease slowly (Fig. 5e). In the initial stage, the rapid decline in the density of the current is caused by the accumulation of toxic intermediate species on the Pd surface, resulting in slow oxidation kinetics and rapid decrease of catalytic activities. After that, the current densities slowly decline until they reach a relatively steady state [2]. Compared with PdPb@rGO/In_2O_3 (33.79 $mA \cdot cm^{-2}$), PdBi@rGO/In_2O_3 (23.79 $mA \cdot cm^{-2}$), Pd@rGO/In_2O_3 (19.43 $mA \cdot cm^{-2}$) and Pd/C (4.03 $mA \cdot cm^{-2}$), PdPbBi@rGO/In_2O_3 maintained improved electrooxidative activity towards EG, and the retained current density (40.47 $mA \cdot cm^{-2}$) still reaches 51.38% of the initial value. The normalized currents of the five catalysts also show the same pattern after 3600 s (Fig. S3). From above results, it is proved that doped alloy NPs can improve the catalytic activity of the catalyst.

Diffusion kinetics and charge transfer of different electrocatalysts on electrode/electrolyte interface were evaluated by measuring Nyquist plot of electrochemical impedance spectroscopy (EIS) (Fig. 5f). Nyquist's arcs are displayed in the following order: PdPbBi@rGO/In_2O_3 (12.68 Ω) < PdPb@rGO/In_2O_3 (13.19 Ω) < PdBi@rGO/In_2O_3 (17.17 Ω) < Pd@rGO/In_2O_3 (18.88 Ω) < Pd/C (35.19 Ω). The smaller the impedance is, the more favorable the transfer of charge is from electrode to fuel, reducing the fuel oxidation activation barrier and the electrode reaction overpotential [62]. EIS results confirm that the trimetallic catalyst PdPbBi@rGO/In_2O_3 exhibits superior charge transfer properties, faster electrochemical kinetics and better catalytic performance than other catalysts.

Figure 6a is the integral area data of PdPbBi@rGO/In_2O_3, PdPb@rGO/In_2O_3, PdBi@rGO/In_2O_3, and Pd@rGO/In_2O_3 catalysts. The integral area (X) was obtained from the reduction peak of oxides appearing from −0.1 to −0.8 V in CV curve in 1.0 mol·L^{-1} KOH electrolyte, and ECSA values were calculated from (X). The integral area of the PdPbBi@rGO/In_2O_3 is larger than that of PdPb@rGO/In_2O_3, PdBi@rGO/In_2O_3, and Pd@rGO/In_2O_3. The normalized area is obtained by comparing the ECSA value to the mass of Pd (Fig. 6b).

Analysis of the above test results showed that the synergistic effect of PdPbBi NPs and rGO/In_2O_3 significantly enhanced its electrocatalytic activity. The excellent electrocatalytic activity of PdPbBi@rGO/In_2O_3 also contributes to the porous structure of rGO/In_2O_3. This enables the Pd-Pb-Bi alloy NPs to be uniformly dispersed with more active sites, thereby accelerating the Pd-Pb-Bi electron transfer from NPs to rGO/In_2O_3. To elucidate the excellent electrocatalytic activity of PdPbBi@rGO/In_2O_3, the electrocatalytic oxidation mechanism of EG is proposed (Scheme 2).

We infer that the removal of $[CO]_{ads}$ facilitated EGOR through several processes [63]:

$$C_2H_6O_2 \rightarrow [C_2H_6O_2]_{ads} \quad (1)$$

$$OH^- \rightarrow [OH^-]_{ads} \quad (2)$$

$$[C_2H_6O_2]_{ads} + 4[OH^-]_{ads} \rightarrow (CHO)(CHO) + 4H_2O + 4e^- \quad (3)$$

$$(CHO)(CHO) + 6[OH^-]_{ads} \rightarrow (COO^-)_2 + 4H_2O + 4e^- \quad (4)$$

$$(COO^-)_2 + 4[OH^-]_{ads} \rightarrow 2CO_3^{2-} + 2H_2O + 2e^- \quad (5)$$

As shown in the above steps, the oxidation mechanism of EG is described as Reactions (1–5). Completely EG oxidation into carbonate ions will produce 10 electrons through a series of C–C and C–H bond breaks [60]. Intermediates such as glyoxal (Reaction (3)) and oxalate ions (Reaction (4)) are produced on the surface of catalysts. This results in partial occupancy of Pd active sites, which slows down electro-oxidative kinetics and reduces electrocatalytic activity [61]. The trimetallic composite PdPbBi@rGO/In_2O_3 exhibits excellent electrocatalytic performance for EGOR due to the columnar structure and abundant $[OH]_{ads}$ obtained from Bi and Pb/PbO NPs [64].

$$2Pd + C_2H_6O_2 + 6OH^- \rightarrow 2[Pd - CO]_{ads} + 6H_2O + 6e^- \quad (6)$$

$$PbO + OH^- \rightarrow [PbOOH]_{ads} + e^- \quad (7)$$

$$Pb + OH^- \rightarrow [PbOH]_{ads} + e^- \quad (8)$$

$$Bi + OH^- \rightarrow [BiOH]_{ads} + e^- \quad (9)$$

$$[PdCO]_{ads} + [PbOOH]_{ads} + 3OH^- \rightarrow Pd + PbO + CO_3^{2-} + 2H_2O + e^- \quad (10)$$

$$[PdCO]_{ads} + [PbOH]_{ads} + 3OH^- \rightarrow Pd + Pb + CO_3^{2-} + 2H_2O + e^- \quad (11)$$

$$[PdCO]_{ads} + [BiOH]_{ads} + 3OH^- \rightarrow Pd + Bi + CO_3^{2-} + 2H_2O + e^- \quad (12)$$

The modified Pd is the catalytically active site. EG adsorbs on the Pd site (Reaction (6)) and dehydrogenates to the $[CO]_{ads}$ intermediate, resulting in deactivation of the Pd catalyst. Because of the higher affinity of Pb/PbO for oxygenated substances, oxidized surfaces such as OH^- species are generated at Pb-Bi site than at Pd site (Reactions (7–9)), forming $[PbOH]_{ads}$ and $[PbOOH]_{ads}$. This would facilitate the conversion of the adsorbed $[CO]_{ads}$ to $CO_3{}^{2-}$ (Reactions (10–12)) in alkaline media, thus making more Pd active sites available for EG oxidation. Furthermore, due to the different electronegativities of Pd, Pb and Bi, charges are transferred from Pb and Bi to the Pd surface. The reduction of the d-band center of Pd is due to this electronic effect between Pd–Pb–Bi. The combination of Pd with Pb and Bi alloys effectively modifies the electronic structure of Pd. This will significantly accelerate the electron transfer rate due to the synergistic effect of Pd–Pb–Bi, thereby increasing the catalytic activity [65]. On the other hand, Pb and Bi co-doping can promote the adsorption and oxidation of intermediate carbon-containing species, accelerate the oxidation elimination of intermediate poisons (especially CO), and enhance the electrochemical stability of EGOR [48]. Apart from that, the support with porous columnar structure and excellent electrical conductivity is favorable to provide larger surface area and loading of alloy NPs. As a result, the binding energy of the active site for CO adsorption and the activation energy for ethylene glycol adsorption oxidation

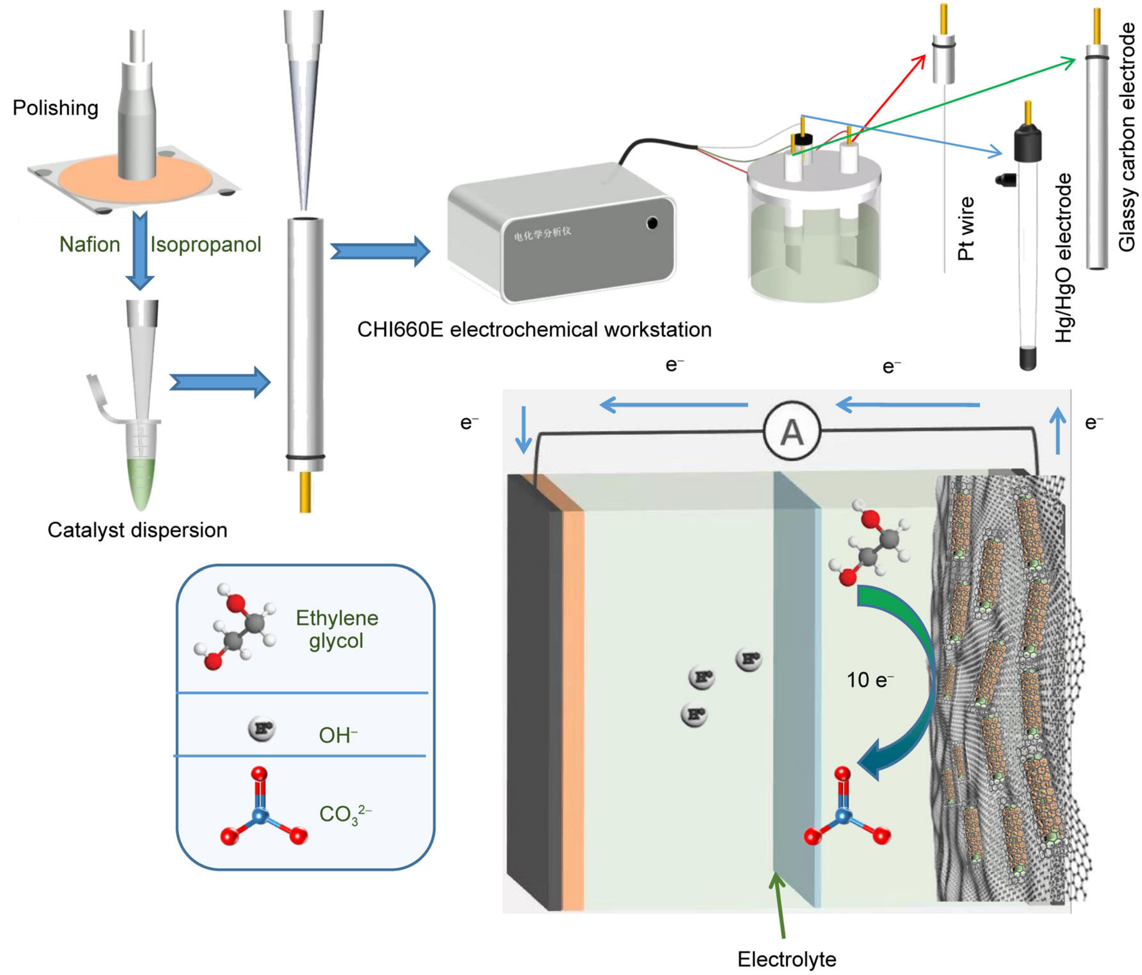

Scheme 2 Electrooxidation mechanism of EG and removal process of $[CO]_{ads}$ on Pd sites

decrease. These results provide important value for the development of high efficiency alcohol-based fuel cell electrocatalysts.

4 Conclusion

The Pd-Pb-Bi nanoalloys were supported on the hydrothermally and calcined precursor rGO/In_2O_3 by reduction method. Then a trimetallic columnar catalyst PdPbBi@rGO/In_2O_3 was obtained, which exhibits excellent electrochemical performance for EGOR. PdPbBi@rGO/In_2O_3 has higher forward current density (229.12 $mA \cdot cm^{-2}$), larger ECSA (85.87 $m^2 \cdot g^{-1}{}_{Pd}$), smaller impedance (12.68 Ω) and smaller E_{onset} (−0.56 V) than commercial Pd/C, Pd@rGO/In_2O_3, PdBi@rGO/In_2O_3 and PdPb@rGO/In_2O_3. Specifically, the current density and ECSA are 8.46 and 3.38 times higher than those of Pd/C (27.07 $mA \cdot cm^{-2}$, 25.41 $m^2 \cdot g^{-1}{}_{Pd}$), respectively. The oxidation mechanism of glycol and the process of CO removal are also discussed. The columnar support structure wrapped by reduced graphene oxide provides a huge active surface area for catalysis. Moreover, the electronic effect among Pd-Pb-Bi nanoalloy particles can accelerate the removal of CO intermediate species, resulting in more Pd active sites and improved electrocatalytic performance. Our first synthesis of this highly electrocatalytic composite material provides a good idea for further commercial application of direct fuel cells.

Acknowledgements This study was financially supported by the Key Laboratory of Organic Functional Molecule Synthesis and Applications, Ministry of Education (No. KLSAOFM1913).

Declarations

Conflict of interests The authors declare that they have no conflict of interest.

References

[1] Jiang MH, Hu Y, Zhang WJ, Wang L, Yang SY, Liang JC, Zhang ZW, Zhang XL, Jin Z. Regulating the alloying degree and electronic structure of Pt-Au nanoparticles for high-efficiency direct C^{2+} alcohol fuel cells. Chem Mater. 2021;33(10):3767. https://doi.org/10.1021/acs.chemmater.1c00886.

[2] Yang T, Zhang CX, Wang ZZ, Bai P, Wang XJ, Chai ZL. Ternary interface of Pt|few-layered N-rGO|TiN for the boasting electrocatalytic activity in ethylene glycol oxidation. Adv Mater Interfaces. 2020;7(20):2000808. https://doi.org/10.1002/admi.202000808.

[3] Sun XD, Li YS, Xie C, Hao MS, Li MJ, Xue JL. Activating triple-phase boundary via building oxygen-electrolyte interfaces to construct high-performance PH-disparate direct liquid fuel cells. Chem Eng J. 2021;418:129480. https://doi.org/10.1016/j.cej.2021.129480.

[4] Logeshwaran N, Panneerselvam IR, Ramakrishnan S, Kumar RS, Kim AR, Wang Y, Yoo DJ. Quasihexagonal platinum nanodendrites decorated over CoS_2-N-doped reduced graphene oxide for electro-oxidation of C1-, C2-, and C3-type alcohols. Adv Sci. 2022;9(8):2105344. https://doi.org/10.1002/advs.202105344.

[5] Kannan R, Kim AR, Nahm KS, Yoo DJ. Manganese-titanium-oxide-hydroxide-supported palladium nanostructures–a facile electrocatalysts for the methanol, ethylene glycol and xylitol electrooxidation. Int J Hydrogen Energy. 2016;41(16):6787. https://doi.org/10.1016/j.ijhydene.2016.03.058.

[6] Park KS, Choi YJ, Kang JG, Sung YM, Park JG. The effect of the concentration and oxidation state of Sn on the structural and electrical properties of indium tin oxide nanowires. Nanotechnology. 2011;22(28):285712. https://doi.org/10.1088/0957-4484/22/28/285712.

[7] Munisamy M, Yang HW, Perumal N, Kang NY, Kang WS, Kim SJ. A flower-like In_2O_3 catalyst derived via metal-organic frameworks for photocatalytic applications. Int J Mol Sci. 2022;23(8):4398. https://doi.org/10.3390/ijms23084398.

[8] Sun LM, Li R, Zhan WW, Yuan YS, Wang XJ, Han XG, Zhao YL. Double-shelled hollow rods assembled from nitrogen/sulfur-codoped carbon coated indium oxide nanoparticles as excellent photocatalysts. Nat Commun. 2019;10:1. https://doi.org/10.1038/s41467-019-10302-0.

[9] Wang YY, Xue SL, Xie P, Gao ZY, Zou RJ. Preparation, characterization and photocatalytic activity of juglans-like indium oxide (In_2O_3) nanospheres. Mater Lett. 2017;192:76. https://doi.org/10.1016/j.matlet.2016.12.057.

[10] Zhang F, Li XY, Zhao QD, Chen AC. Facile and controllable modification of 3D In_2O_3 microflowers with In_2S_3 nanoflakes for efficient photocatalytic degradation of gaseous ortho-dichloro benzene. J Phys Chem C. 2016;120(34):19113. https://doi.org/10.1021/acs.jpcc.6b03618.

[11] Li HH, Chen C, Huang XY, Leng Y, Hou MN, Xiao XG, Bao J, You JL, Zhang WW, Wang YK, Song J, Wang YP, Liu QQ, Hope GA. Fabrication of In_2O_3@In_2S_3 core-shell nanocubes for enhanced photoelectrochemical performance. J Power Sources. 2014;247:915. https://doi.org/10.1016/j.jpowsour.2013.09.054.

[12] Wang YC, Sun ZS, Wang SZ, Wang SY, Cai SX, Huang XY, Li K, Chi ZT, Pan SD, Xie WF. Sub-ppm acetic acid gas sensor based on In_2O_3 nanofibers. J Mater Sci. 2019;54(22):14055. https://doi.org/10.1007/s10853-019-03877-y.

[13] Zhao Y, Liu J, Han ML, Yang GP, Ma LF, Wang YY. Two comparable Ba-MOFs with similar linkers for enhanced CO_2 capture and separation by introducing N-rich groups. Rare Met. 2021;40(2):499. https://doi.org/10.1007/s12598-020-01597-w.

[14] Yang FL, Zhao PP, Hua X, Luo W, Cheng GZ, Xing W, Chen SL. A cobalt-based hybrid electrocatalyst derived from a carbon nanotube inserted metal-organic framework for efficient water-splitting. J Mater Chem A. 2016;4(41):16057. https://doi.org/10.1039/c6ta05829a.

[15] Singh BK, Lee S, Na K. An overview on metal-related catalysts: metal oxides, nanoporous metals and supported metal nanoparticles on metal organic frameworks and zeolites. Rare Met. 2020;39(7):751. https://doi.org/10.1007/s12598-019-01205-6.

[16] Dai HW, Zhou WJ, Wang W. Co/N co-doped carbonaceous polyhedron as efficient peroxymonosulfate activator for degradation of organic pollutants: role of cobalt. Chem Eng J. 2021;417:127921. https://doi.org/10.1016/j.cej.2020.127921.

[17] Ezeigwe ER, Dong L, Wang JY, Wang LL, Yan W, Zhang JJ. MOF-deviated zinc-nickel-cobalt ZIF-67 electrode material for high-performance symmetrical coin-shaped supercapacitors. J Colloid Interface Sci. 2020;574:140. https://doi.org/10.1016/j.jcis.2020.04.025.

[18] Zhai JR, Kang QL, Liu QY, Lai DW, Lu QY, Gao F. In-situ generation of In_2O_3 nanoparticles inside $In[Co(CN)_6]$ quasi-metal-organic-framework nanocubes for efficient electroreduction of CO_2 to formate. J Colloid Interface Sci. 2022;608:1942. https://doi.org/10.1016/j.jcis.2021.10.096.

[19] Tsumori N, Chen LY, Wang QJ, Zhu QL, Kitta M, Xu Q. Quasi-MOF: exposing inorganic nodes to guest metal nanoparticles for drastically enhanced catalytic activity. Chem. 2018;4(4):845. https://doi.org/10.1016/j.chempr.2018.03.009.

[20] Shi XX, Xu H, Wu Y, Zhao Y, Meng HM, Li Z, Qu L. Two-dimension (2D) Cu-MOFs/aptamer nanoprobe for in situ ATP imaging in living cells. J. Anal. Test. 2021;5:165. https://doi.org/10.1007/s41664-021-00172-1.

[21] Wang ZJ, Li Q, Tan LL, Liu CG, Shang L. Metal–organic frameworks-mediated assembly of gold nanoclusters for sensing applications. J. Anal. Test. 2022. https://doi.org/10.1007/s41664-022-00224-0.

[22] Yuan JJ, Liu W, Zhang XK, Zhang YH, Yang WT, Lai WD, Li XK, Zhang JJ, Li XF. MOF derived ZnSe-$FeSe_2$/RGO nanocomposites with enhanced sodium/potassium storage. J Power Sources. 2020;455:227937. https://doi.org/10.1016/j.jpowsour.2020.227937.

[23] Zhang XP, Huang L, Wang QQ, Dong SJ. Transformation of homobimetallic MOFs into nickel-cobalt phosphide/nitrogen-doped carbon polyhedral nanocages for efficient oxygen evolution electrocatalysis. J Mater Chem A. 2017;5(35):18839. https://doi.org/10.1039/c7ta06272a.

[24] Guan BY, Yu L, Lou XW. General synthesis of multishell mixed-metal oxyphosphide particles with enhanced electrocatalytic activity in the oxygen evolution reaction. Angew Chem Int Edit. 2017;56(9):2386. https://doi.org/10.1002/anie.201611804.

[25] Wang D, Chang YX, Li YR, Zhang SL, Xu SL. Well-dispersed $NiCoS_2$ nanoparticles/rGO composite with a large specific surface area as an oxygen evolution reaction electrocatalyst. Rare Met. 2021;40(11):3156. https://doi.org/10.1007/s12598-021-01733-0.

[26] Serov A, Kwak C. Recent achievements in direct ethylene glycol fuel cells (DEGFC). Appl Catal B-Environ. 2010;97:1. https://doi.org/10.1016/j.apcatb.2010.04.011.

[27] Zhang SJ, Liu L, Yang JY, Zhang YQ, Wan ZR, Zhou LQ. Pd-Ru-Bi nanoalloys modified three-dimensional reduced graphene oxide/MOF-199 composites as a highly efficient electrocatalyst for ethylene glycol electrooxidation. Appl Surf Sci. 2019;492:617. https://doi.org/10.1016/j.apsusc.2019.06.228.

[28] Zhang RL, Duan JJ, Han Z, Feng JJ, Huang H, Zhang QL, Wang AJ. One-step aqueous synthesis of hierarchically multi-branched

PdRuCu nanoassemblies with highly boosted catalytic activity for ethanol and ethylene glycol oxidation reactions. Appl Surf Sci. 2020;506:144791. https://doi.org/10.1016/j.apsusc.2019.144791.

[29] Li ZJ, Chen YF, Fu GT, Chen Y, Sun DM, Lee JM, Tang YW. Porous PdRh nanobowls: facile synthesis and activity for alkaline ethanol oxidation. Nanoscale. 2019;11(6):2974. https://doi.org/10.1039/c8nr09482a.

[30] Kumar TR, Kumar GG, Manthiram A. Biomass-derived 3D carbon aerogel with carbon shell-confined binary metallic nanoparticles in CNTs as an efficient electrocatalyst for microfluidic direct ethylene glycol fuel cells. Adv Energy Mater. 2019;9(16):1803238. https://doi.org/10.1002/aenm.201803238.

[31] Huang C, Wang X, Wang D, Zhao W, Bu K, Xu J, Huang X, Bi Q, Huang J, Huang F. Atomic pillar effect in Pd_xNbS_2 to boost basal plane activity for stable hydrogen evolution. Chem Mater. 2019;31(13):4726. https://doi.org/10.1021/acs.chemmater.9b00821.

[32] Wang D, Wang X, Lu Y, Song C, Pan J, Li C, Sui M, Zhao W, Huang F. Atom-scale dispersed palladium in a conductive $Pd_{0.1}TaS_2$ lattice with a unique electronic structure for efficient hydrogen evolution. J Mater Chem A. 2017;5(43):22618. https://doi.org/10.1039/C7TA06447K.

[33] Fang Y, Wang S, Zhang X, Lin G, Zhao W, Wang X, Wang W, Huang F. Realizing the excellent HER performance of $Pt_3Pb_2S_2$ by d-orbital electronic modulation. Inorg Chem. 2021;60(21):16538. https://doi.org/10.1021/acs.inorgchem.1c02422.

[34] Fang Y, Wang S, Lin G, Wang X, Huang F. A new compound $Pt_3Bi_2S_2$ with superior performance for the hydrogen evolution reaction. Chem Commun. 2021;57(64):7946. https://doi.org/10.1039/D1CC02741G.

[35] Ma N, Wang SQ, Liu XH, Sun YC, Yin YR, Zhang LY, Guo PZ. PdPb bimetallic nanowires as electrocatalysts for enhanced ethanol electrooxidation. Sci China Mater. 2020;63(10):2040. https://doi.org/10.1007/s40843-020-1350-7.

[36] Lv H, Lopes A, Xu DD, Liu B. Multimetallic hollow mesoporous nanospheres with synergistically structural and compositional effects for highly efficient ethanol electrooxidation. ACS Central Sci. 2018;4(10):1412. https://doi.org/10.1021/acscentsci.8b00490.

[37] Xiong ZP, Xu H, Li SM, Gu ZL, Yan B, Guo J, Du YK. Concave Pd-Ru nanocubes bounded with high active area for boosting ethylene glycol electrooxidation. Appl Surf Sci. 2018;427:83. https://doi.org/10.1016/j.apsusc.2017.08.170.

[38] Jia Y, Li F, Fan K, Sun L. Cu-based bimetallic electrocatalysts for CO_2 reduction. Adv Powder Mater. 2022;1(1):100012. https://doi.org/10.1016/j.apmate.2021.10.003.

[39] Qian X, Wei Y, Sun M, Han Y, Zhang X, Tian J, Shao M. Heterostructuring 2D TiO_2 nanosheets in situ grown on $Ti_3C_2T_x$ MXene to improve the electrocatalytic nitrogen reduction. Chin J Catal. 2022;43(7):1937. https://doi.org/10.1016/S1872-2067(21)64020-2.

[40] Qian X, Ma C, Shahid UB, Sun M, Zhang X, Tian J, Shao M. Synergistic enhancement of electrocatalytic nitrogen reduction over few-layer $MoSe_2$-decorated $Ti_3C_2T_x$ MXene. ACS Catalysis. 2022;12(11):6385. https://doi.org/10.1021/acscatal.2c01172.

[41] Hummers WS, Offeman RE. Preparation of graphitic oxide. J Am Chem Soc. 1958;80(6):1339. https://doi.org/10.1021/ja01539a017.

[42] Wu P, Huang YY, Zhou LQ, Wang YB, Bu YK, Yao JN. Nitrogen-doped graphene supported highly dispersed palladium-lead nanoparticles for synergetic enhancement of ethanol electrooxidation in alkaline medium. Electrochim Acta. 2015;152:68. https://doi.org/10.1016/j.electacta.2014.11.110.

[43] Sun M, Li FL, Su MJ, Wei D, Yang QQ, Yan T, Li DZ. Fabrication of MOF-derived tubular $In_2O_3@SnIn_4S_8$ hybrid: heterojunction formation and promoted photocatalytic reduction of Cr (VI) under visible light. J Colloid Interface Sci. 2021;596:278. https://doi.org/10.1016/j.jcis.2021.02.121.

[44] Wang SB, Guan BY, Lou XW. Construction of $ZnIn_2S_4$-In_2O_3 hierarchical tubular heterostructures for efficient CO_2 photoreduction. J Am Chem Soc. 2018;140(15):5037. https://doi.org/10.1021/jacs.8b02200.

[45] Shamraiz U, Ahmad Z, Raza B, Badshah A, Ullah S, Nadeem MA. CaO- promoted graphene-supported palladium nanocrystals as a universal electrocatalyst for direct liquid fuel cells. ACS Appl Mater Interfaces. 2020;12(4):4396. https://doi.org/10.1021/acsami.9b16151.

[46] Ramakrishnan S, Velusamy DB, Sengodan S, Nagaraju G, Kim DH, Kim AR, Yoo DJ. Rational design of multifunctional electrocatalyst: an approach towards efficient overall water splitting and rechargeable flexible solid-state zinc-air battery. Appl Catal B-Environ. 2022;300:120752. https://doi.org/10.1016/j.apcatb.2021.120752.

[47] Kannan R, Kim AR, Nahm KS, Lee HK, Yoo DJ. Synchronized synthesis of Pd@C-RGO carbocatalyst for improved anode and cathode performance for direct ethylene glycol fuel cell. Chem Commun. 2014;50(93):14623. https://doi.org/10.1039/c4cc06879c.

[48] Dong QZ, Wu MM, Mei DH, Shao YY, Wang Y, Liu J, Li HZ, Hong LY. Multifunctional Pd-Sn electrocatalysts enabled by in situ formed SnO_x and TiC triple junctions. Nano Energy. 2018;53:940. https://doi.org/10.1016/j.nanoen.2018.08.060.

[49] Chen L, Lu LL, Zhu HL, Chen YG, Huang Y, Li YD, Wang LY. Improved ethanol electrooxidation performance by shortening Pd-Ni active site distance in Pd-Ni-P nanocatalysts. Nat Commun. 2017;8:1. https://doi.org/10.1038/ncomms14136.

[50] Chen MH, Zhou LQ, Lu D, Li Y, Ning HH, Pan YX, Xu HK, Peng WW, Zhang SR. RuCo bimetallic alloy nanoparticles immobilized on multi-porous MIL-53(Al) as a highly efficient catalyst for the hydrolytic reaction of ammonia borane. Int J Hydrogen Energy. 2018;43(3):1439. https://doi.org/10.1016/j.ijhydene.2017.11.160.

[51] Choi M, Ahn CY, Lee H, Kim JK, Oh SH, Hwang W, Yang S, Kim J, Kim OH, Choi I, Sung YE, Cho YH, Rhee CK, Shin W. Bi-modified Pt supported on carbon black as electro-oxidation catalyst for 300 W formic acid fuel cell stack. Appl Catal B--Environ. 2019;253:187. https://doi.org/10.1016/j.apcatb.2019.04.059.

[52] Wang YD, Ding JN, Zhao J, Wang JJ, Han XP, Deng YD, Hu WB. Selective electrocatalytic reduction of CO_2 to formate via carbon-shell-encapsulated In_2O_3 nanoparticles/graphene nanohybrids. J Mater Sci Technol. 2022;121:220. https://doi.org/10.1016/j.jmst.2022.01.006.

[53] Wang J, Sun KH, Jia XY, Liu CJ. CO_2 hydrogenation to methanol over Rh/In_2O_3 catalyst. Catal Today. 2021;365:341. https://doi.org/10.1016/j.cattod.2020.05.020.

[54] Zhang JB, Yin RG, Shao Q, Zhu T, Huang XQ. Oxygen vacancies in amorphous InO_x nanoribbons enhance CO_2 adsorption and activation for CO_2 electroreduction. Angew Chem Int Edit. 2019;58(17):5609. https://doi.org/10.1002/anie.201900167.

[55] Wu J, Li XD, Shi W, Ling PQ, Sun YF, Jiao XC, Gao S, Liang L, Xu JQ, Yan WS, Wang CM, Xie Y. Efficient visible-light-driven CO_2 reduction mediated by defect-engineered BiOBr atomic layers. Angew Chem Int Edit. 2018;57(28):8719. https://doi.org/10.1002/anie.201803514.

[56] Lei FC, Sun YF, Liu KT, Gao S, Liang L, Pan BC, Xie Y. Oxygen vacancies confined in ultrathin indium oxide porous

sheets for promoted visible-light water splitting. J Am Chem Soc. 2014;136(19):6826. https://doi.org/10.1021/ja501866r.

[57] Ren F, Chen X, Xing R, Du Y. Rod-like MnO_2 boost Pd/reduced graphene oxide nanocatalyst for ethylene glycol electrooxidation. J Colloid Interface Sci. 2021;582:561. https://doi.org/10.1016/j.jcis.2020.07.133.

[58] Hong JW, Kim Y, Wi DH, Lee S, Lee SU, Lee YW, Choi SI, Han SW. Ultrathin free-standing ternary-alloy nanosheets. Angew Chem Int Edit. 2016;55(8):2753. https://doi.org/10.1002/anie.201510460.

[59] Qi Z, Geng HR, Wang XG, Zhao CC, Ji H, Zhang C, Xu JL, Zhang ZH. Novel nanocrystalline PdNi alloy catalyst for methanol and ethanol electro-oxidation in alkaline media. J Power Sources. 2011;196(14):5823. https://doi.org/10.1016/j.jpowsour.2011.02.083.

[60] Wan ZR, Bai X, Mo H, Yang JY, Wang Z, Zhou LQ. Multi-porous NiAg-doped Pd alloy nanoparticles immobilized on reduced graphene oxide/$CoMoO_4$ composites as a highly active electrocatalyst for direct alcohol fuel cell. Colloid Surface A. 2021;614:126048. https://doi.org/10.1016/j.colsurfa.2020.126048.

[61] Askari MB, Salarizadeh P, Di Bartolomeo A, Zadeh MHR, Beitollahi H, Tajik S. Hierarchical nanostructures of $MgCo_2O_4$ on reduced graphene oxide as a high-performance catalyst for methanol electro-oxidation. Ceram Int. 2021;47(11):16079. https://doi.org/10.1016/j.ceramint.2021.02.182.

[62] Xu H, Wang J, Yan B, Li SM, Wang CQ, Shiraishi Y, Yang P, Du YK. Facile construction of fascinating trimetallic PdAuAg nanocages with exceptional ethylene glycol and glycerol oxidation activity. Nanoscale. 2017;9(43):17004. https://doi.org/10.1039/c7nr06737b.

[63] Wang Y, Nguyen TS, Liu XW, Wang X. Novel palladium-lead (Pd-Pb/C) bimetallic catalysts for electrooxidation of ethanol in alkaline media. J Power Sources. 2010;195(9):2619. https://doi.org/10.1016/j.jpowsour.2009.11.072.

[64] Zhong YT, Hu YL, Mo H, Wu ZR, Fu X, Zhou LQ, Liu HY, Li L, Liu XG. Facilitation of PdPb nanoalloy anchored on rGO/MOF-derived δ-Ga_2O_3 nanorod for electrocatalytic oxidation of methanol, ethanol and ethylene glycol. Electrochim Acta. 2022;408:139935. https://doi.org/10.1016/j.electacta.2022.139935.

[65] Zhang JX, Zhao TK, Yuan ML, Li ZH, Wang WB, Bai YL, Liu ZJ, Li SW, Zhang GJ. Trimetallic synergy in dendritic intermetallic PtSnBi nanoalloys for promoting electrocatalytic alcohol oxidation. J Colloid Interface Sci. 2021;602:504. https://doi.org/10.1016/j.jcis.2021.06.028.